Moiré patterns in van der Waals heterostructures

Maxime Le Ster,[1] Tobias Maerkl,[1] Pawel J. Kowalczyk,[2] and Simon A. Brown[1,*]

[1]*The MacDiarmid Institute for Advanced Materials and Nanotechnology, Department of Physics and Astronomy, University of Canterbury, Private Bag 4800, Christchurch 8140, New Zealand*

[2]*Department of Solid State Physics, Faculty of Physics and Applied Informatics, University of Lodz, 90-236 Lodz, Pomorska 149/153, Poland*

(Received 21 December 2018; published 15 February 2019)

Using scanning tunneling microscopy, we report the observation of moiré patterns (MPs) on van der Waals heterostructures comprised of various 2D allotropes of bismuth and antimony grown on highly ordered pyrolytic graphite and MoS_2. The spatial periods of the MPs range from $\lambda \sim 1$ to ~ 10 nm. For all the reported cases (α-bismuthene, α-antimonene, β-antimonene, and monolayer bismuthene), we model the observations using a simple superposition model (SSM). Where possible, the results obtained from the SSM are compared to analytical prediction. MPs emerging from mixed symmetry stacking (hexagonal on rectangular) are explained without requiring commensuration of the layers.

DOI: 10.1103/PhysRevB.99.075422

I. INTRODUCTION

The isolation of graphene [1,2] and other atomically thin crystals (h-BN [3], MoS_2 [4], Si [5], Ge [6], P [7,8], Sn [9], etc.) has led to an explosion of interest in two-dimensional (2D) materials. A large library of 2D crystals exists, with a wide range of electronic properties ranging from metallic to insulating [10]. Many of these materials offer unprecedented mechanical, thermal, and optical properties [11] providing a platform for, for example, extreme miniaturization of electronic, biomedical, and spintronic [12–14] devices.

The intralayer bonding within a 2D crystal is typically covalent, but multilayer systems are bound via much weaker van der Waals interactions. Stacked to the desired sequence, the 2D materials—acting as building blocks—form so-called van der Waals heterostructures (VDWHs) [11,15,16]. VDWHs can be prepared rather simply (the absence of strong interlayer interactions permits the superposition of virtually any given pair of 2D layers) using either *bottom-up* or *top-down* approaches. The former makes use of successive deposition techniques steps while the latter requires the fabrication of the individual layers first, and subsequent peel off and assembly [11].

In VDWHs, the lack of strong interlayer bonding facilitates device engineering through a new degree of freedom, the twist angle θ between two 2D crystals. This rotation causes the formation of moiré patterns (MPs), which can drastically alter the properties of the VDWH. A good example is bilayer graphene where a variety of electronic effects can be achieved by manipulating θ: unconventional superconducting and Mott insulator states can be engineered at the "magic angle" $\theta = 1.1^\circ$ [17], Dirac cones can be shifted within the first Brillouin zone [18], van Hove singularities [19,20] and fractal Hofstadter [21] "butterfly" energy spectra [22–25] can be designed, and incommensurate quasicrystalline structures can be created at $\theta = 30^\circ$ [26,27]. Similarly, in h-BN/graphene heterostructures θ can tune the band gap [28–30].

Our primary interest, and motivation for the present work, is the potential for MPs to provide a platform for topological device engineering, and specifically to use MPs to modulate local strain and therefore design, for example, spin-polarized current channels [31]. Moreover, thorough analysis of the MPs can reveal information on the interplanar interactions [32], and can act as a "magnifying lens" for observing structural defects in 2D crystals [30,33]. The investigation of these effects is still in its infancy, and one of the reasons for this is that there is currently no standard formalism for predicting or interpreting observed MPs arising from generalized symmetry stacking. Here we discuss a simple and readily implemented procedure that can be used for any pair of 2D materials, and show its application to a range of heterostructures built from group-V elements, which are strong candidates for topological devices.

A. Observation of moiré patterns

The most direct way of observing MPs in VDWHs is usually through scanning tunneling microscopy (STM). MPs appear as a periodic height modulation in STM images. The vast majority of the reported examples of MPs arise from hexagonal lattices superposed onto other hexagonal lattices, e.g., on multilayered graphene/graphite systems [18,19,23,34–36], Pb on Ag(111) [37], graphene on h-BN [28–30], on Ir(111) [38], on Cu(111) [39], etc. More rarely, the interfering crystalline structures (*under-* and *overlayer*) possess a rectangular symmetry, e.g., Bi on GaAs(110) [40], NaCl on Ag(100) [41], twisted bilayer phosphorene [42], or monolayer Bi (MBi) on α-Bi [43]. Our reports on group-V compounds on HOPG and MoS_2 [44,45] constitute, to the best of our knowledge, the only experimental reports focusing on the MPs generated by a mixed symmetry stacking (e.g., rectangular and hexagonal symmetries). The analysis of MPs in these mixed symmetry systems is particularly challenging.

*Corresponding author: simon.brown@canterbury.ac.nz

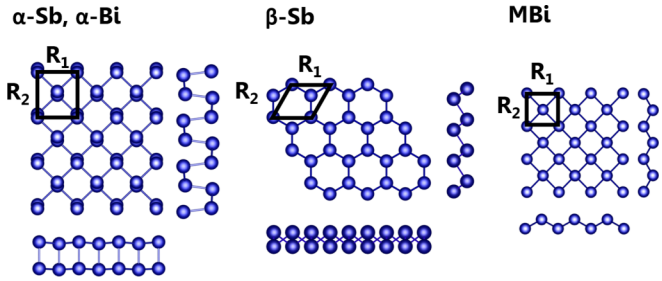

FIG. 1. Ball-and-stick models of the different allotropes of Bi and Sb that are observed in our experiments (α-Bi and α-Sb, β-Sb, and MBi) showing both top and side views. The unit cells are indicated in black. The literature lattice parameters are given in Table I. Note that the notation used in the literature can be confusing and so for clarity we emphasize that in the present paper: the thickness of the paired-layer α phase indicated here is two monolayers (2 ML), whereas the β-Sb and MBi structures are both 1-ML thick.

The appearance of the MPs depends on several factors [36]: the strength of the interaction between the layers, the distance between the tip and the surface, and the bias voltage at which the image is recorded, but it is clear that the twist angle θ between the layers will also be important. STM images in which MPs are present can in principle be calculated if the detailed atomic structure is known [36,46], but in the case of incommensurate structures this is extremely challenging due to the absence of true periodicity. Similarly, in the case of long range commensurability an enormous unit cell is required.

B. Topological group-V materials

Group-V elemental and alloy crystals have attracted significant attention since the first fabrication of black-phosphorous-based transistors [7] and the discovery that $Bi_{1-x}Sb_x$ is a three-dimensional (3D) topological insulator [47,48]. Because of the strong spin-orbit coupling in Bi, many of its known allotropes are topologically nontrivial: α-Bi [49,50], β-Bi [51], and even bulk Bi [52] have all been reported to possess nontrivial topology, and most recently exotic hinge states have been reported in Bi nanowires [53]. An area of active investigation is whether the topological properties survive in the low-dimensional forms of these materials [45,50]. In fact the 2D forms of these materials are interesting because of the crystalline symmetries that are adopted. Figure 1 shows the α phase ("black-phosphorus"-like, A17 group) consisting of two paired layers with an atom near the middle of the rectangular unit cell, the β phase which has a buckled honeycomb structure, and the unusual rectangular MBi phase [43].

α-Bismuthene (α-Bi) has been extensively investigated [44,54–63] and is of particular relevance to the present work because Sb allotropes are grown on top of islands of α-Bi. The low-dimensional phases of antimonene (Sb) have been much less investigated: first-principles calculations were reported several years ago [64–66], but experimental realizations of β-Sb [67–70] and α-Sb [45,70,71] were only reported more recently. Topologically protected edge states are predicted for α-Sb [45], multilayer β-Sb [72,73], and sufficiently strained monolayer β-Sb [74]. Table I compiles the literature lattice constants of the different materials studied here, as well as the substrates on which they are grown.

TABLE I. Literature values of the lattice constants R_1, R_2 of the various group-V 2D allotropes. The indicated value of α-Bi is for a paired layer (2-ML α-Bi) grown on HOPG [56]. The bulk values are $R_1 \times R_2 = 4.54 \times 4.75$ Å^2 [76]. The nature of the underlayer onto which these layers are observed in this paper is also indicated. The type of stacking symmetry is indicated as X on Y (R: rectangular, H: hexagonal).

Layer	α-Bi [56]	α-Sb [45]	β-Sb [45]	MBi [43]
R_1 (Å)	4.5 ± 0.2	4.29 ± 0.09	4.04 ± 0.04	4.0 ± 0.2
R_2 (Å)	4.8 ± 0.2	4.86 ± 0.10	4.04 ± 0.04	4.1 ± 0.3
Underlayer	HOPG, MoS_2	4-ML α-Bi	2-ML α-Bi	2-ML α-Bi
Symmetry	R/H	R/R	H/R	R/R

C. The structure of this paper

There is currently no established method for interpreting or modeling the geometry (i.e., the direction and period) of the MPs observed from any pair of 2D layers. In this paper we present an STM study of MPs observed for VDWHs consisting of different 2D allotropes of Bi and Sb. We demonstrate that the geometry of all the MPs observed in our experiments can be explained by the use of a simple superposition model (SSM) which can be applied to all the observed crystal symmetries. Whenever possible, results obtained from the SSM are compared to a previous analytical model [75] which has only a limited range of applicability (see below). Finally, we discuss the observations and modeling and point out that the observed MPs have the longest wavelengths possible, most likely to minimize elastic deformation energy.

II. EXPERIMENTAL AND MODELING

The experiments are performed in an Omicron VT-AFM STM/growth chamber ($P \leqslant 5 \times 10^{-10}$ mbar). Bi and Sb are sequentially deposited from high purity (5N) source materials in heated PBN crucibles. The mechanically cleaved substrates (HOPG or MoS_2) are degassed at $T = 800$ K for at least 2 h and are kept at room temperature during deposition. The tips are obtained from cut Pt/Ir wires. The STM scans are performed at room temperature in the same chamber, maintaining UHV conditions between deposition and analysis. To measure the lattice constants and the geometry of the MPs (essentially the spatial period λ and angle of the fringes δ with respect to a given lattice vector), we use fast-Fourier transforms (FFTs) of STM images. The characterization of the MPs is based on a large number of STM images from multiple islands, and then averaged in order to minimize the effect of thermal drift. The uncertainty in the measurements of λ and δ originate from three different factors: (i) the lateral extension of the islands (i.e., the number of moiré fringes that are visible), (ii) the deviation of the MPs from a plane wave (arising due to local strain or dislocations), and (iii) the statistical variance from multiple measurements. All measurements are calibrated with atomically resolved STM images of HOPG or MoS_2 in all trace directions. The twist angle θ is measured through

comparison of the FFTs of atomically resolved STM images of the under- and overlayer. Where atomic resolution is not available for the overlayer (rotated MBi case, see Sec. III D), θ is determined from the simulations.

To understand the MPs, we use two methods: a simple superposition model (SSM) and an analytical model [75]. While approaches similar to our SSM have previously been applied in an ad-hoc way to several all-hexagonal systems [23,33,35,77–80], here we demonstrate a consistent methodology that can in principle be applied to any system including those with mixed symmetry. MPs observed on α-Bi grown on HOPG have been successfully modeled previously using a commensurate model [44].

A. Simple superposition model

Simulations using the SSM are performed with the freely available software package VESTA [81]. To illustrate the method, we first simulate the MP originating from two systems: (i) twisted bilayer graphene (where both layers have hexagonal symmetry and identical lattice constant) and (ii) α-Bi on HOPG (mixed symmetry). Figures 2(a) and 2(d) show the geometry of the two systems: the underlayer is defined by its unit vectors $\mathbf{R_1}$ and $\mathbf{R_2}$, and the unit cell angle ω, the overlayer (unit vectors $\mathbf{R'_1}, \mathbf{R'_2}$ and unit cell angle ω') is rotated by θ with respect to $\mathbf{R_1}$. For (i) the two graphene layers are rotated by $\theta = 5.0°$, and for (ii) we use the observed value from experiments of $\theta = 30°$ (see Sec. III A below). Figures 2(b) and 2(e) show the underlayer (black) and overlayer (orange) but to identify the MPs one must observe the layers at a larger scale [Figs. 2(c) and 2(f)]. For the twisted bilayer graphene, the MP appears as a superlattice of circular spots, where $\mathbf{R_{M1}}$ and $\mathbf{R_{M2}}$ correspond to the superlattice vectors as indicated in Fig. 2(c) (note that we use the same vectorial notation as in [75] for consistency). We define the period λ as the distance between two rows of spots (fringes), and δ is the angle of the row of spots (fringes) with respect to one of the two layers' unit vectors. Both λ and δ are measured manually using the built-in tools in VESTA. For the first case the SSM yields $\lambda = 2.44$ nm and $\delta_1 = 32.5°$. Interestingly, the MP appears very differently for α-Bi on HOPG [Fig. 2(f)]: instead of a superlattice of spots, only a single periodicity given by $\mathbf{R_{M1}}$ is observed. The SSM shows that the period for $\theta = 30°$ is $\lambda = 3.48$ nm and the fringes are perpendicular to α-Bi $\mathbf{R'_1}$ (white arrow), i.e., $\delta = 90.0°$.

The underlying assumptions of the SSM are the following: (i) the layers are rigid, i.e., there is no relaxation and the under- and overlayer are strictly defined by their respective basis vectors, (ii) the phase of the superposition (i.e., a possible lateral shift of the overlayer with respect to the underlayer) is unimportant as it does not affect the essential features (λ and δ) of the MP, and (iii) the lattice mismatch leads to an *apparent* height modulation and the question of whether the observed MPs originate from purely electronic effects or physical corrugation of the heterostructure (or a combination of the two) is not considered here.

B. Analytical modeling

An analytical model for prediction of the MP for incommensurate superposition was reported previously [75]. The

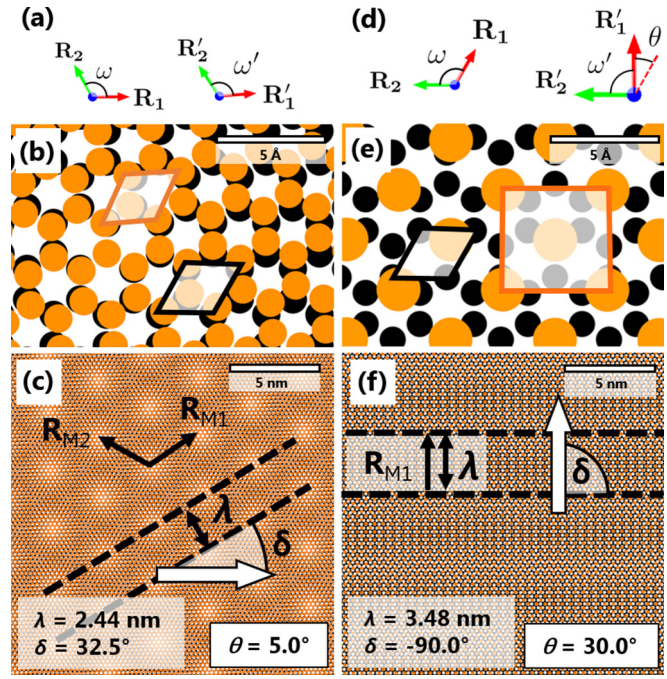

FIG. 2. Unit cell vectors, MP vectors, and SSM, using the examples of twisted bilayer graphene (a)–(c) and the experimentally observed lattice constants of α-Bi on HOPG (d)–(f). (a) and (d) Underlayer (left) and overlayer (right) basis vectors. The lattice constants of the under- (over-) layer are referred to as R_1, R_2 (R'_1, R'_2). The angles ω and ω' define the symmetry of the layers. Here we use in (a)–(c) $R_1 = R_2 = R'_1 = R'_2 = 2.46$ Å and $\omega = \omega' = 2\pi/3$ with a twist angle $\theta = 5.0°$. In (d)–(f) we use the bulk values of Bi ($R'_1 \times R'_2 = 4.54 \times 4.75$ Å^2) on HOPG ($R_1 = R_2 = 2.46$ Å). The overlayer is rotated by $\theta = 30.0°$ with respect to $\mathbf{R_1}$. (b) and (e) SSM where the underlayer (black) and overlayer (orange) are displayed with VESTA. The unit cells are indicated. (c) Large scale SSM, where the MP appears as a superlattice of spots (MP vectors: $\mathbf{R_{M1}}$, $\mathbf{R_{M2}}$). The period λ and angle δ are indicated. For $\theta = 5.0°$, the SSM yields $\lambda = 2.44$ nm and $\delta = 32.5°$. (f) Large scale SSM, where the MP appears as a series of fringes running horizontally. The unique $\mathbf{R_{M1}}$ vector is indicated, as well as the period λ and angle δ with respect to α-Bi $\mathbf{R'_1}$. The SSM yields $\lambda = 3.48$ nm and $\delta = 90.0°$. In (c) and (f) the dashed lines indicate the row of MP spots or fringes and serve as a guide to the eye. The white arrows in (c) and (f) represent the reference vectors from which the angles δ are measured.

MP is defined with the two previously described vectors $\mathbf{R_{M1}}$ and $\mathbf{R_{M2}}$, usually much larger than the unit vectors of the under- and overlayers. In the case of rectangular layers, i.e., $\omega = \omega' = \pi/2$, the expression for $\mathbf{R_{M1}}$ and $\mathbf{R_{M2}}$ is

$$\begin{pmatrix} \mathbf{R_{M1}} \\ \mathbf{R_{M2}} \end{pmatrix} = \frac{1}{\Delta} \begin{pmatrix} p_1 \cos\theta & q p_1 \sin\theta \\ -\frac{1}{q} p_2 \sin\theta & p_2 \cos\theta \end{pmatrix} \begin{pmatrix} \mathbf{R_1} \\ \mathbf{R_2} \end{pmatrix}, \quad (1)$$

where $p_1 = R'_1/R_1$, $p_2 = R'_2/R_2$, $q = R_1/R_2$, and $\Delta = 1 + p_1 p_2 - (p_1 + p_2)\cos\theta$. Equation (1) gives the MP superlattice vectors as a function of θ and of the lattice constants. The range of the validity of the model [75] is limited by the following conditions: (i) the two layers must have an identical unit cell angle $\omega = \omega'$, (ii) the twist angle θ must be within $-10°$ and $+10°$, and (iii) the lattice mismatch cannot exceed

~20%. Due to these limitations, the analytical model can be used for only a subset of the observed cases: α-Sb on α-Bi (see Sec. III B) and MBi on α-Bi (see Sec. III D). For the other cases, α-Bi on HOPG or MoS_2 (see Sec. III A) and β-Sb on α-Bi (see Sec. III C), we use SSMs to understand the experimental observations.

III. RESULTS

We now report experimental results and modeling of the observed MPs for a number of VDWHs.

A. α-Bismuthene

The system of interest consists of 2-ML-thick α-Bi islands grown on two different substrates, with different lattice constants HOPG and MoS_2. We first focus on the MPs observed on α-Bi on HOPG. Figure 3(a) shows an atomically resolved STM image of a 2-ML-thick α-Bi island. Clearly a strong height modulation corresponding to the MP is visible. Two fringes are indicated with dashed lines for clarity. Figure 3(b) shows the FFT of the STM image in Fig. 3(a). The reciprocal lattice points α-Bi (0,1), (1,0) are resolved, as well as the wave-vector **K** corresponding to the MP visible in real space. The measured lattice constants of α-Bi are $R_1' \times R_2' = 4.5 \times 4.8$ Å^2, in agreement (within uncertainties) with bulk values [76] and previous measurements of α-Bi [49,56]. The measurement of the period and angle of the MP, obtained from the average of 40 scans, yield $\lambda = 3.2 \pm 0.4$ nm and $\delta = -54 \pm 5°$.

HOPG and α-Bi do not share the same unit cell angle ($\omega \neq \omega'$), and so the existing analytical model cannot be used to simulate the observations and so we use the SSM as described in Sec. II. First, we use the bulk lattice constants of Bi ($R_1' \times R_2' = 4.54 \times 4.75$ Å^2 [76]), the measured twist angle ($\theta = 30°$), and the literature lattice constants of HOPG ($R_1 = R_2 = 2.46$ Å [82]) [shown in Fig. 2(f)]. The simulation yields $\lambda = 3.48$ nm and $\delta = -90°$. While the period λ agrees relatively well with the observations, the fringe angle δ does not. A refinement of the simulation is then performed. Since the experimental lattice constants and twist angle θ have measurement uncertainties, it is possible to modify the values of R_1', R_2', and θ in the SSM within the uncertainty range until the simulated period and angle agree with the observations. Figure 3(c) shows the simulation [on the same scale as the STM image in Fig. 3(a)] obtained using $R_1' \times R_2' = 4.520 \times 4.750$ Å^2 and $\theta = 28.1°$. These minimal changes to the lattice constants (R_1' reduced by 0.02 Å only) and to the twist angle (θ reduced by 1.9°) yield $\lambda = 3.20$ nm and $\delta = -54.4°$, which are both in very good agreement with the observation. Note that the optimized lattice constants and twist angle are still within the experimental uncertainties.

We now focus on the MPs observed when α-Bi is deposited on MoS_2 substrates. It is clear that since HOPG and MoS_2 have different lattice parameters, the MP structure is expected to differ. Figure 3(d) shows an atomically resolved STM image of a 2-ML-thick α-Bi grown on MoS_2. A clear MP (M_1) is imaged, with fringes running nearly vertically in the image (green lines). Upon closer inspection, two distinct series of fringes M_2 and M_3 with shorter periods and different angles

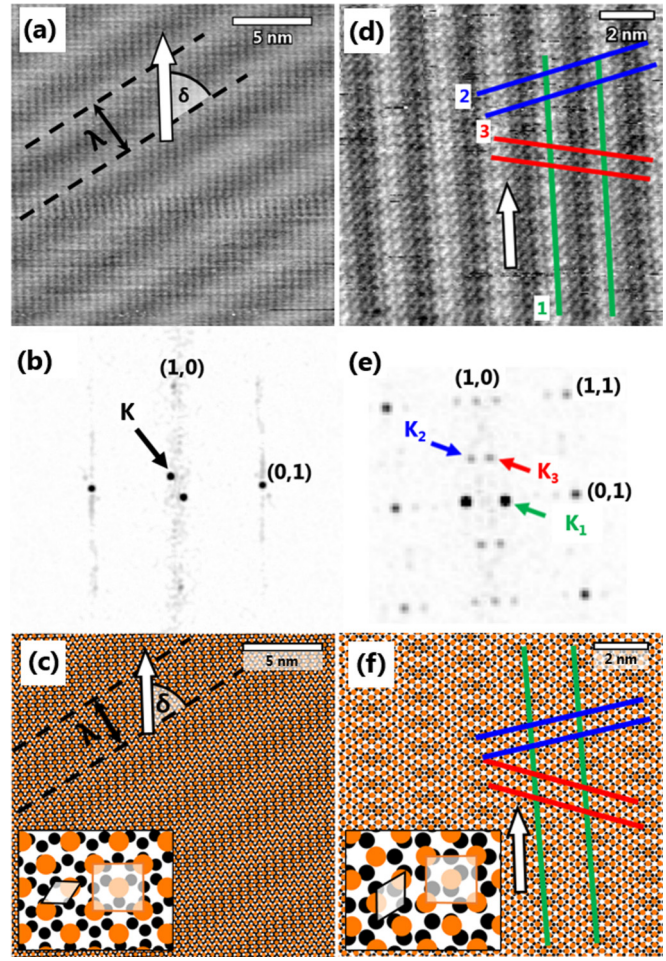

FIG. 3. α-Bi on HOPG (a)–(c) and on MoS_2 (d)–(f). (a) STM topography image ($V = 0.50$ V, $I = 0.90$ nA) of α-Bi grown on HOPG where a clear MP is resolved. The period λ and angle δ. (b) FFT of the STM image in (a). The reciprocal vectors of α-Bi (0,1) and (1,0) and the wave-vector **K** associated with the MP are resolved. (c) SSM of α-Bi on HOPG using $R_1 = 2.46$ Å, $R_1' \times R_2' = 4.520 \times 4.750$ Å^2 for a twist angle of $\theta = 28.1°$. (d) STM topography image ($V = 0.05$ V, $I = 30$ pA) of α-Bi grown on MoS_2. Three distinct MPs (M_1, M_2, and M_3) are resolved, the fringes are indicated respectively with green, blue, and red lines. (e) FFT of the STM image in (d), where the reciprocal vectors (1,0), (0,1) and (1,1) of α-Bi and $\mathbf{K_1}$, $\mathbf{K_2}$, and $\mathbf{K_3}$ are indicated. (f) SSM of α-Bi on MoS_2, using $R_1 = 3.161$ Å, $R_1' \times R_2' = 4.530 \times 4.870$ Å^2 twisted by $\theta = 0.3°$. The insets in (c) and (f) show the SSMs at higher magnification where the unit cells of the underlayer (black) and overlayer (orange) are indicated. The white arrows indicate the $\mathbf{R_1'}$ α-Bi direction, chosen as a reference for the measurement of δ.

are also resolved (blue and red lines). Figure 3(e) shows the FFT of the STM image in Fig. 3(d). The (0,1), (1,0), and (1,1) points of the reciprocal lattice are resolved. More importantly, the FFT shows the three distinct wave vectors $\mathbf{K_1}$, $\mathbf{K_2}$, and $\mathbf{K_3}$ that correspond to the three MPs observed in the real-space image. Inspection of the FFT in Fig. 3(e) leads to the observation that the wave vectors of the MPs are related by $\mathbf{K_1} = \mathbf{K_3} - \mathbf{K_2}$, i.e., the MPs M_2 and M_3 have similar wave vectors and interfere to create M_1. Repeated imaging

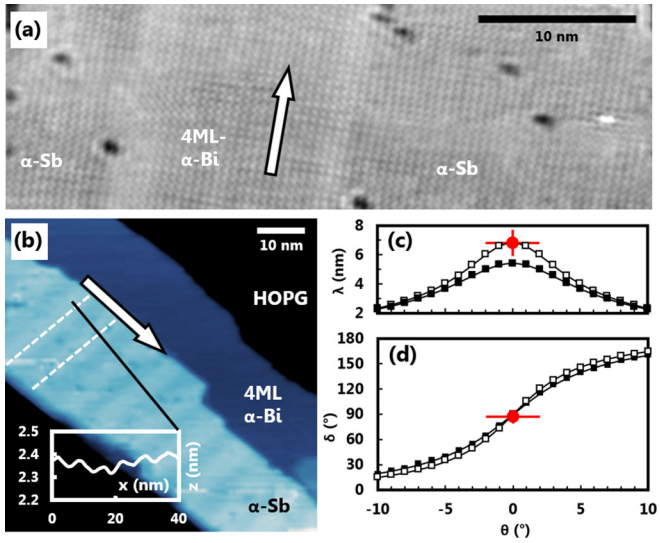

FIG. 4. (a) Atomically resolved STM image ($V = 0.1$ V, $I = 50$ pA) of a α-Sb layer grown on a 2-ML α-Bi layer in which a 4-ML α-Bi stripe separates laterally the two α-Sb layers. (b) STM topography image ($V = 1.0$ V, $I = 20$ pA) of a α-Sb layer (light blue) grown on a 4-ML-thick α-Bi island (dark blue). A clear fringelike MP is visible, the fringes running nearly perpendicular to the α-Bi $\mathbf{R_1}$ direction (white arrow). [Inset: Topography profile extracted from the black line in (a). The period is $\lambda = 6.8 \pm 0.9$ nm, and the fringe angle $\delta = 87 \pm 8°$.] (c) and (d) Moiré period λ (c) and fringe angle δ (d) using the experimental (solid squares) and optimized lattice constants (open squares) using systematic SSMs. Observed (red), and analytically calculated (solid lines) λ and δ are also added.

and analysis performed on multiple islands yield $\lambda_1 = 2.22 \pm 0.07$ nm, $\delta_1 = 4 \pm 2°$, $\lambda_2 = 0.99 \pm 0.05$ nm, $\delta_2 = -79 \pm 2°$, and $\lambda_3 = 1.00 \pm 0.05$ nm, $\delta_3 = 75 \pm 2°$.

Figure 3(f) shows the SSM using the experimental lattice constants for both MoS_2 and α-Bi for the twist angle $\theta = 0.3°$. Here $\lambda_1 = 2.20$ nm, $\delta_1 = 2.7°$, $\lambda_2 = 1.03$ nm, $\delta_2 = -77.2°$, and $\lambda_3 = 1.00$ nm, $\delta_3 = 76.1°$, which are in very good agreement with the experimental values. For this case, no modification is required of either the lattice constants or twist angle to agree with the observations.

B. α-Antimonene

The black-phosphorus-like allotrope of antimonene, α-Sb [45], is only observed on top of either 2-ML-thick or 4-ML-thick α-Bi structures. Figure 4(a) shows an example of an atomically resolved STM image of two α-Sb structures grown on a 2-ML α-Bi layer, where the two α-Sb structures (left and right of the image) are separated by a narrow 4-ML α-Bi stripe. Clearly this image shows that the α-Bi and α-Sb layers are aligned ($\theta = 0 \pm 2°$). The measured lattice constants of a 4-ML α-Bi are $R_1 \times R_2 = 4.53 \pm 0.10 \times 4.87 \pm 0.10$ Å^2, which are similar to those measured on a 2-ML α-Bi (see Table I). Despite the small change in the lattice constants, neither the atomic structures nor the MPs differ significantly when the underlayer's thickness is changed and so we only discuss the MPs generated by the stacking of α-Sb on a 4-ML α-Bi.

Figure 4(b) shows a STM topography image of a typical α-Sb layer (light blue) grown on a 4-ML α-Bi layer (dark blue), itself deposited on HOPG (black). The lattice parameters of α-Sb on a 4-ML α-Bi are $R'_1 \times R'_2 = 4.18 \times 4.84$ Å^2, slightly differing from those measured on α-Sb on a 2-ML α-Bi. Clearly a fringelike MP is visible, where the fringes extend nearly perpendicular to the α-Bi $\mathbf{R_1}$ direction (indicated with a white arrow). The inset in Fig. 4(a) shows the topographic profile obtained from the black line in the STM image, which reveals a peak-to-peak amplitude of ~1 Å. The average period is $\lambda = 6.8 \pm 0.9$ nm and the angle of the fringes (with respect to α-Bi $\mathbf{R_1}$) is $\delta = 87 \pm 8°$.

We now focus on modeling the MP using the SSM. The lattices of both α-Bi and α-Sb are generated using the experimentally observed lattice constants as shown in Table I and simulated images (not shown) are obtained for a range of twist angles consistent with the measurement uncertainty in θ. Figure 4(c) shows the simulated period λ (solid squares) as a function of θ in the range $-10° \leqslant \theta \leqslant 10°$ (in steps of 1°). The experimentally observed period λ is also plotted (red). The simulated period peaks at $\lambda = 5.41$ nm for $\theta = 0$. Clearly, whichever the value of θ, the simulated period is too small to agree with the observations. The simulated (solid square) and experimental (red) fringe angles δ are plotted in Fig. 4(d), and both agree for $\theta = 0 \pm 2°$. However, because the period obtained in the experiment and in the SSM do not agree, the MP cannot be explained with the experimentally observed unit cells of both α-Bi and α-Sb. We therefore repeat the SSMs using slightly modified unit cells (within the measurement uncertainties listed in Table II).

To increase the simulated period, the lattice mismatch in the direction perpendicular to the MP fringes $R'_1 - R_1$ must be decreased. The open squares in Figs. 4(c) and 4(d) show, respectively, the simulated period and angle obtained with using $R_1 \times R_2 = 4.497 \times 4.870$ Å^2 and $R'_1 \times R'_2 = 4.218 \times 4.840$ Å^2. For $\theta = 0$ the period is $\lambda = 6.80$ nm and $\delta = 90°$, which is in excellent agreement with the observed MP. The fringe angle δ is not significantly affected by the small change in the unit cells and still agrees well with the experimental value of $\delta = 87°$. For completeness, because the conditions for analytical predictions are met ($10° \leqslant \theta \leqslant 10°$ and $\omega = \omega' = \pi/2$) we test the validity of the SSM method by analytically calculating the MPs using the analytical formalism detailed in Sec. II B, both using experimental and optimized lattice constants. The curves of both λ and δ are plotted along with the simulated periods and angles in Figs. 4(c) and 4(d) (solid lines). Clearly the SSM method and the analytical prediction agree very well.

Finally, we note that while in principle a second MP is possible in the direction perpendicular to the MP observed in Fig. 4(b), the near zero lattice mismatch in that direction (~0.6%) would lead to a period of $\lambda \sim 78.6$ nm which would not be visible in the present experiments due to the limited width of the α-Sb layers (typically ~20 nm). It is also possible in this case that the weak strain experienced by α-Sb is released leading to a change in the MP.

TABLE II. Lattice constants R_1', R_2', twist angles θ, MP periods λ, and angles δ obtained for all the studied VDWHs. In each case, experimentally determined values are shown on the first line, and values obtained from modeling are shown between parentheses on the second line. All values used in SSMs agree with the observations within the measurement uncertainties. Note the minute differences between the 2-ML α-Bi lattice constants when grown on HOPG versus MoS_2. Note, for the 2-ML α-Bi/MoS_2 case, $\lambda_3 = 1.00 \pm 0.05$ nm (1.00 nm using SSM) and $\delta_3 = 75 \pm 2^\circ$ (76.1° using SSM).

Overlayer	2-ML α-Bi	2-ML α-Bi	α-Sb	β-Sb	MBi
Underlayer	HOPG	MoS_2	4-ML α-Bi	2-ML α-Bi	2-ML α-Bi
R_1' (Å)	4.5 ± 0.2	4.53 ± 0.05	4.18 ± 0.09	4.04 ± 0.04	4.0 ± 0.2
	(4.520)	(4.530)	(4.218)	(4.080)	(3.97)
R_2' (Å)	4.8 ± 0.2	4.87 ± 0.04	4.84 ± 0.10	4.04 ± 0.04	4.1 ± 0.3
	(4.750)	(4.870)	(4.840)	(4.080)	(3.82)
θ (deg)	30 ± 5	0.3 ± 0.6	0 ± 2	12 ± 3	1 ± 3
	(28.1)	(0.3)	(0.00)	(12.5)	(0.5)
λ_1 (nm)	3.2 ± 0.4	2.22 ± 0.07	6.8 ± 0.9	4.7 ± 0.5	1.9 ± 0.2
	(3.20)	(2.20)	(6.80)	(4.57)	(1.95)
δ_1 (deg)	-54 ± 5	4 ± 2	87 ± 8	-39 ± 8	2.5 ± 2.0
	(−54.4)	(2.7)	(90.0)	(−36.1)	(2.6)
λ_2 (nm)	NA	0.99 ± 0.05	NA	1.06 ± 0.06	3.1 ± 0.3
	NA	(1.03)	NA	(1.05)	(3.16)
δ_2 (deg)	NA	-79 ± 2	NA	37 ± 6	-80 ± 10
	NA	(−77.2)	NA	(33.9)	(−86.0)

C. β-Antimonene

The hexagonal allotrope of antimonene, β-Sb, is observed only on top of 2-ML-thick α-Bi nanostructures [45], regardless of whether Bi is first deposited onto HOPG or MoS_2 substrates. Figure 5(a) shows an STM image of β-Sb (blue) on the α-Bi island (dark blue) grown on a MoS_2 substrate. A MP, labeled M_1, is visible (dashed white lines). The average value for the period is $\lambda_1 = 4.7 \pm 0.5$ nm and the fringe angle with respect to the $\mathbf{R_1}$ vector of α-Bi is $\delta_1 = -39 \pm 8^\circ$. Figure 5(b) shows an atomically resolved STM image of a different instance of β-Sb, also grown on 2-ML-thick α-Bi on MoS_2 substrate. At this resolution, another distinct MP (referred to as M_2) is visible, and is characterized by $\lambda_2 = 1.06 \pm 0.06$ nm and $\delta_2 = 37 \pm 6^\circ$. The FFT of the STM image in Fig. 5(b) is shown in Fig. 5(c). The (1,0) and (0,1) reciprocal lattice vectors of β-Sb (and their linear combinations) and the wave vectors associated with M_1 and M_2 ($\mathbf{K_1}$ and $\mathbf{K_2}$, indicated with black and blue arrows) are resolved.

Similar to the α-Bi/HOPG and α-Bi/MoS_2 cases in Sec. III A, the under- and overlayer do not share the same symmetry ($\omega = \pi/2 \neq \omega' = 2\pi/3$), and the twist angle $\theta > 10^\circ$ so the use of the analytical model is not permitted, and one can only model the MP using the SSM. The procedure is identical to that developed in Sec III A: first, the two lattices α-Bi and β-Sb are superposed, using the experimentally observed lattice constants and the measured twist angle $\theta = 12.0^\circ$ (not displayed here). The simulation leads to $\lambda_1 = 6.11$ nm, $\delta_1 = -30.6^\circ$ and $\lambda_2 = 1.05$ nm, $\delta_2 = 38.7^\circ$. While the simulated MPs are already in the right ballpark, λ_1 is significantly larger than the observed $\lambda_1 = 4.7 \pm 0.5$ nm. The lattice constants and/or twist angle used for the simulations must therefore be modified until an agreement is found with the observations. Due to the large parameter space that can be varied within the simulations (R_1, R_2, R_1', R_2', θ), we first varied only the twist angle θ and recorded the simulated periods and angles of M_1 and M_2, conserving the lattice constants as measured. Figure 6(a) shows the simulated δ_1 as a function of the simulated period λ_1, for the twist angles ranging from $\theta = 9.0^\circ$ to 15.0° with a step angle $\Delta\theta = 0.5^\circ$ (solid squares). As θ is increased, the value of λ_1 increases until $\theta \sim 12.5^\circ$ and then decreases. Conversely δ_1 decreases rather steadily from $\theta = 9.0^\circ$ to $\theta = 15.0^\circ$. However, there is no value of θ that can model accurately both the observed λ_1 and δ_1 (red symbol). The lattice parameters used in the SSM have to be modified in order to reduce the simulated λ_1.

New simulations are therefore performed using the SSM, this time varying the lattice parameters (with the condition that R_1, R_2, R_1' are kept within their experimental uncertainties). The periods and angles of M_1 and M_2 are systematically recorded. Figure 6(a) shows the values (λ_1, δ_1) obtained for the optimized lattice parameters $R_1 \times R_2 = 4.48 \times 4.83$ Å^2 and $R_1' = 4.08$ Å (in open squares). Now the SSM data agrees with the observed values (in red) for the twist angle $\theta = 12 \pm 1^\circ$. For $\theta = 12.5^\circ$ the SSM yields $\lambda_1 = 4.57$ nm, $\delta_1 = -36.1^\circ$ which are in close agreement with the observations. The optimized SSM is shown in Fig. 5(d), where several moiré fringes of M_1 and M_2 (respectively, white and blue dashed lines) are indicated. The inset of Fig. 5(d) shows the SSM at higher magnification. The direct visualisation of both the STM image in Fig. 5(b) and the simulation using the SSM in Fig. 5(d) further confirms the agreement.

Figure 6(b) shows the values (λ_2, δ_2) obtained from the SSM using the experimentally observed (black squares) and the optimized lattice parameters (open squares). In contrast to M_1, the values of both simulated λ_2 and δ_2 do not depend strongly on θ. The scatter in simulated λ_2, δ_2 is a result of the manual approach of the SSM technique, as it can be difficult to accurately visualize the periodic change of contrast constituted by the M_2 fringes on screen [see Fig. 5(d)]. Nevertheless, the small range in which the values of λ_2 and δ_2 scatter agrees well with the observed M_2 (red symbol).

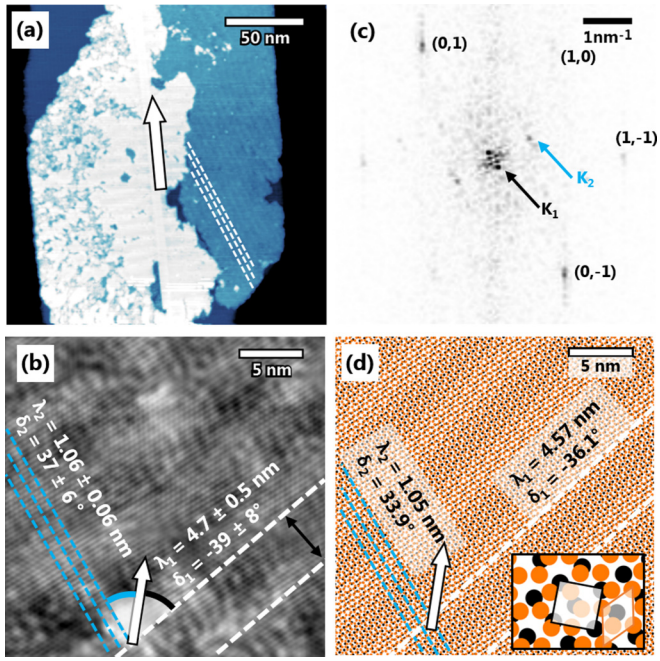

FIG. 5. (a) STM topographic image ($V = 0.20$ V, $I = 10$ pA) of a VDWH grown on MoS_2 (black). β-Sb (blue) is present on top of the 2-ML-thick α-Bi island (dark blue). A MP (M_1) is visible on the β-Sb layer. (b) Atomically resolved STM image ($V = 0.10$ V, $I = 50$ pA) of β-Sb, where both M_1 (highlighted with white dashed lines, $\lambda_1 = 4.7 \pm 0.5$ nm, $\delta_1 = -39 \pm 8°$) and M_2 (blue dashed lines, $\lambda_2 = 1.06 \pm 0.06$ nm, $\delta_2 = 37 \pm 6°$) are resolved. (c) FFT of the STM image in (b). The reciprocal vectors of β-Sb (1,0), (0,1), and (1, −1) are indicated. The FFT resolves both $\mathbf{K_1}$ (black arrow) and $\mathbf{K_2}$ (blue arrow), the wave vectors associated, respectively, with M_1 and M_2. In (a), (b), and (d), α-Bi $\mathbf{R'_1}$ is indicated (white arrow). (d) SSM of β-Sb (orange) on α-Bi (black), using $R_1 \times R_2 = 4.480 \times 4.830$ Å^2 and $R'_1 = R'_2 = 4.080$ Å, for a twist angle $\theta = 12.5°$, leading to two simulated MPs M_1 ($\lambda_1 = 4.57$ nm, $\delta_1 = -36.1°$, indicated with white dashed lines) and M_2 ($\lambda_2 = 1.05$ nm, $\delta_1 = 33.9°$, indicated with blue dashed lines). The inset in (d) is a higher magnification of the SSM where the unit cells are indicated.

D. Monolayer bismuthene

A previously unpredicted single monolayer, rectangular allotrope of bismuthene (MBi), has recently been realized [43]. MBi is only $\sim 2 \pm 1$ Å thick when observed on 2-ML-thick α-Bi islands, confirming that it is comprised of a single atomic layer. Figure 7(a) shows an atomically resolved STM image, revealing the MBi unit cell of $R'_1 \times R'_2 = 4.0 \pm 0.2 \times 4.1 \pm 0.2$ Å^2. Two moiré fringes are also resolved: M_1 ($\lambda_1 = 1.9 \pm 0.2$ nm, $\delta_1 = 2.5 \pm 2.0°$ indicated with black dashed lines) and M_2 ($\lambda_2 = 3.1 \pm 0.3$ nm, $\delta_2 = -80 \pm 10°$, indicated with blue dashed lines). Again, the fringe angles δ are measured with respect to the underlying 2-ML α-Bi $\mathbf{R_1}$ direction (white arrow). The preferential growth direction of the 4-ML α-Bi stripes seen in large scale images (see below) allows us to directly measure the twist angle θ between MBi and α-Bi. The MBi and α-Bi crystals are in fact nearly aligned, as $\theta = 1 \pm 3°$.

Figure 7(b) shows a different MBi layer (blue) grown on a 2-ML α-Bi (black) existing between two 4-ML α-Bi stripes

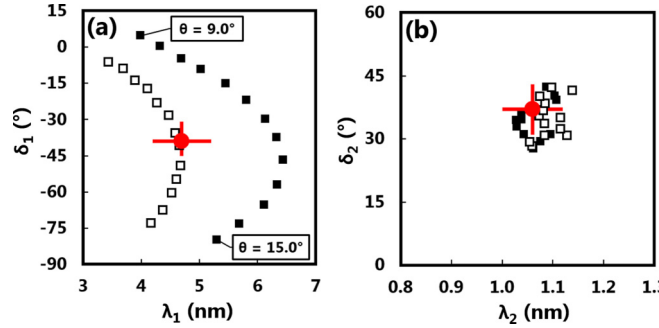

FIG. 6. (a) Fringe angle δ_1 versus period λ_1 and (b) δ_2 versus λ_2 obtained from SSMs using the experimentally observed lattice constants ($R_1 \times R_2 = 4.53 \times 4.87$ Å^2 and $R'_1 = 4.04$ Å, solid squares) and optimized lattice constants ($R_1 \times R_2 = 4.48 \times 4.83$ Å^2 and $R'_1 = 4.08$ Å, open squares). The observed M_1 (λ_1, δ_1) and M_2 (λ_2, δ_2) are added onto the graph (red). In both panels the twist angle step is $\Delta\theta = 0.5°$.

(white). The α-Bi lattice vector $\mathbf{R_1}$ is indicated with the white arrow. The direction of the 4-ML α-Bi stripes is also used to obtain θ as previously discussed. A MP (dashed black lines) is visible, and is characterized by the same period λ_1 and angle δ_1 as in Fig. 7(a), i.e., 1.9 nm and 2.5°, respectively. Figure 7(c) shows the same region as in Fig. 7(b) after tip modification (TM). Clearly the changes due to TM led to a reduction of the lateral extension of the layer, and induced a variety of defects corresponding to the darker patches on the topographic image. However, the MP fringes are still visible, and are characterized with $\lambda'_1 = 1.9 \pm 0.3$ nm and $\delta'_1 = 20 \pm 4°$. Unfortunately, the imaging conditions could neither allow resolution of M_2 in Figs. 7(b) and 7(c), nor the atomic structure in Fig. 7(c).

We now focus on the modeling of the MPs, for the three experimental images in Figs. 7(a)–7(c). We simulate the MPs using the SSM with the experimentally observed lattice parameters of both 2-ML α-Bi and MBi for the observed twist angle $\theta = 1°$ (not shown). Two distinct MP fringes are observed, qualitatively similar to the STM image in Fig. 7(a). The SSM yields $\lambda_1 = 2.97$ nm, $\delta_1 = 7.3°$, $\lambda_2 = 3.33$ nm, $\delta_2 = -80.6°$. While M_2 is in very good agreement with the observation, the simulated M_1 fringes are too large and appear excessively rotated with respect to $\mathbf{R_1}$. The simulation is therefore systematically repeated by varying θ from $-10°$ to 10°. The simulated values of (λ_1, δ_1) and (λ_2, δ_2) are collected and displayed in Fig. 7(d) (solid squares, black for M_1, blue for M_2). The observed MPs, M_1 and M_2 (before TM) and M'_1 (after TM) are also plotted (red symbols). Clearly the simulated MPs do not agree with the observed ones for the entire studied range: rather, the SSM-derived periods, in particular λ_1, are too large. The lattice mismatch between α-Bi and MBi must therefore be increased to reduce the period. SSMs are repeated with a slightly compressed MBi unit cell until the agreement is satisfactory. The open squares in Fig. 7(d) show the SSM results using the optimized unit cell for MBi ($R_1 \times R_2 = 3.97 \times 3.82$ Å^2). Note that the unit cell for α-Bi remains unchanged and consistent with previous examples. For $\theta = 0.5°$: the new simulated MPs are $\lambda_1 =$

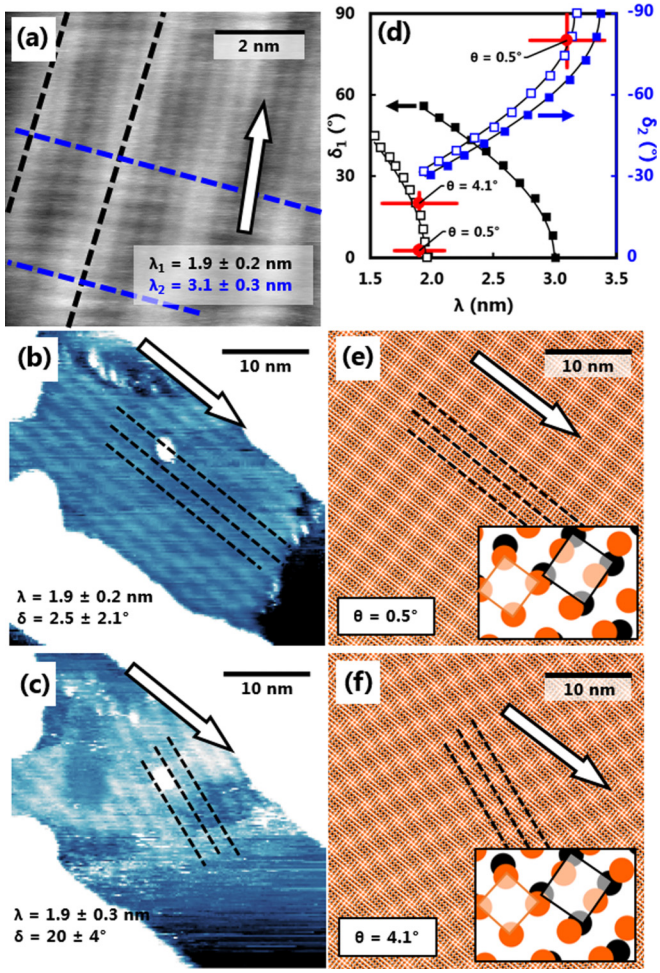

FIG. 7. (a) Atomically resolved STM image ($V = -0.8$ V, $I = 0.2$ nA) of a MBi layer grown on a 2-ML α-Bi. The α-Bi reference lattice vector $\mathbf{R_1}$ is indicated (white arrow). Clearly a dual fringelike MP is observed, and the periods λ_1 and λ_2 are indicated on the figure. (b) STM image ($V = -0.8$ V, $I = 0.1$ nA) of a MBi layer (blue) grown on a 2-ML α-Bi (black) between two 4-ML α-Bi stripes (white). Only M_1 is visible (black dashed lines). (c) STM image ($V = -0.8$ V, $I = 0.1$ nA, RT) of the same area obtained after tip modification. M_1 appears rotated by about 20° with respect to $\mathbf{R_1}$. (d) SSM-derived fringe angle δ as a function of λ for both M_1 (black) and M_2 (blue), using the experimentally observed lattice constants (solid squares) and after optimization (open squares lines). The experimentally observed MPs are displayed in red. (e) SSM of the MBi layer (orange) on α-Bi (black) in (b) for an angle of $\theta = 0.5°$. (f) SSM for an angle of $\theta = 4.1°$. Insets in (e) and (f) show the SSMs in higher resolution. The unit cells are indicated.

1.95 nm, $\delta_1 = 2.6°$ and $\lambda_2 = 3.16$ nm, $\delta_2 = -86.0°$ which are all in very good agreement with the observed MPs before TM. Figure 7(e) shows the simulated MPs for $\theta = 0.5°$. The M_1 fringes are indicated with black dashed lines, and it is clear that the result from the SSM agrees with the STM image in Fig. 7(b). For the value of $\theta = 4.1°$, the simulated M_1 has a period $\lambda_1' = 1.85$ nm and $\delta_1' = 20.3°$ which agrees very well with the observed M_1' after TM. Figure 7(f) shows the result from the optimized SSM for $\theta = 4.1°$. Here too, the agreement with the STM image in Fig. 7(c) is clear. Despite the lack of atomic resolution data, it is possible to understand the MPs both before and after TM: the MBi layer was rotated by $\theta = 4.1 - 0.5 = 3.6°$ relative to the α-Bi underlayer.

IV. DISCUSSION AND CONCLUSION

Our approach to understanding observed moiré patterns is based on a simple superposition model. The SSM allows an understanding of the origin of the MPs in all the VDWHs studied here and we believe that the same approach should be applicable to any VDWH. Table II summarizes the final parameters that described the MPs observed for α-Bi on HOPG and MoS_2 substrates, as well as for α-Sb on α-Bi, β-Sb on α-Bi, and MBi on α-Bi. The results of the SSM are in good agreement with the only available analytical model [75], in the few cases where that model is applicable.

The SSM also allows an understanding of the evolution of the MPs as the twist angle θ between the two layers is varied. More generally, modeling the observed MPs in this way allows precise determination of the structure of both under- and overlayer. The SSM allows corrections to the lattice constants and/or twist angle θ in order to precisely model the periods and angles of all the observed MP fringes.

While the method relies on manual measurement of the periods and angles, the SSM appears to be the first consistent approach to understanding of MPs for layer structures that do not share the same symmetry, and has the advantage that it does not require commensurability. A general analytical model remains to be developed, and would be of significant benefit to the design of VDWHs.

The visualization of the MPs produced by the SSM requires some thought and experience. Obviously rendering parameters chosen in software, such as the diameter of the atoms, can affect the clarity of the MPs on screen. We also find that the screen resolution is important in viewing generated images as aliasing effects can occur if the wrong resolution is chosen; high definition rendering is preferred. Additionally, including both atoms within the unit cell for the BP-like structures (α phases in Fig. 1) increases the visual contrast in many cases (Figs. 1 and 2). These visualization issues do not impact on the geometry of the MPs (the measured period or fringe angle) except in the case of MBi/α-Bi (Fig. 7), where the inclusion of the middle atom in the unit cell generates images (not shown) in which an additional MP resulting from the interference of the diagonal rows of atoms is observed strongly. We hypothesize that this difference with the experimental images is related to the strong atomic buckling of the MBi, in which the middle atom is vertically offset by ~1.5 Å [43], and therefore does not participate in the bilayer interaction that leads to the observed MP.

We have carefully considered the question of whether the solutions provided by the SSM are unique. For each case we explored a wide range of simulated patterns and examined the trends in the simulated period λ and angle δ as θ was varied. These are continuous functions (as shown in Figs. 4, 6, and 7) and it is therefore possible to be confident that other solutions do not exist. We note that in some cases a range of the lattice constants could be used in the SSMs to yield the required λ

and δ. However the choice of these parameters is restricted by the experimental lattice constants and we only consider values within the range of the experimental uncertainties.

Finally, we note that in all the examples discussed here the overlayer adopts a rotational configuration in which the period is very close to the maximum possible ($\theta \sim 0$ for MBi/α-Bi, α-Sb/α-Bi, and α-Bi/MoS_2, $\theta \sim 12.5^\circ$ for β-Sb/α-Bi, and for $\theta \sim 30^\circ$ for α-Bi/HOPG). The simplest interpretation of this observation is to that the overlayer, which has a rotational degree of freedom (θ), rotates during the early stage of growth in order to minimize the elastic deformation energy due to the lattice mismatch between the layers.

ACKNOWLEDGMENTS

This work was supported by the Marsden Fund (UOC1503, M.L.S., T.M., and S.A.B.), the MacDiarmid Institute for Advanced Materials and Nanotechnology (M.L.S., T.M., and S.A.B.), and the Polish National Science Centre (DEC-2015/17/B/ST3/02362, P.J.K.).

[1] K. S. Novoselov, A. K. Geim, S. V. Morozov, D. Jiang, Y. Zhang, S. V. Dubonos, I. V. Grigorieva, and A. A. Firsov, Science **306**, 666 (2004).
[2] K. S. Novoselov, A. K. Geim, S. V. Morozov, D. Jiang, M. I. Katsnelson, I. V. Grigorieva, S. V. Dubonos, and A. A. Firsov, Nature (London) **438**, 197 (2005).
[3] K. Watanabe, T. Taniguchi, and H. Kanda, Nat. Mater. **3**, 404 (2004).
[4] K. F. Mak, C. Lee, J. Hone, J. Shan, and T. F. Heinz, Phys. Rev. Lett. **105**, 136805 (2010).
[5] B. Lalmi, H. Oughaddou, H. Enriquez, A. Kara, S. Vizzini, B. Ealet, and B. Aufray, App. Phys. Lett. **97**, 223109 (2010).
[6] M. E. Dávila, L. Xian, S. Cahangirov, A. Rubio, and G. L. Lay, New J. Phys. **16**, 095002 (2014).
[7] L. Li, Y. Yu, G. J. Ye, Q. Ge, X. Ou, H. Wu, D. Feng, X. H. Chen, and Y. Zhang, Nat. Nanotech. **9**, 372 (2014).
[8] H. Liu, A. T. Neal, Z. Zhu, Z. Luo, D. Xu, X. Tománek, and P. D. Ye, ACS Nano **8**, 4033 (2014).
[9] S. Saxena, R. P. Chaudhary, and S. Shukla, Sci. Rep. **6**, 31073 (2016).
[10] D. Geng and H. Y. Yang, Adv. Mater. **30**, 1800865 (2018).
[11] K. S. Novoselov, A. Mishchenko, A. Carvalho, and A. H. Castro Neto, Science **353**, aac9439 (2016).
[12] H. Shen, L. Zhang, M. Liu, and Z. Zhang, Theranostics **2**, 283 (2012).
[13] K. Kostarelos and K. S. Novoselov, Science **344**, 261 (2014).
[14] W. Han, APL Mater. **4**, 032401 (2016).
[15] A. K. Geim and I. V. Grigorieva, Nature (London) **499**, 419 (2013).
[16] Y. Liu, N. O. Weiss, X. Duan, H.-C. Cheng, Y. Huang, and X. Duan, Nat. Rev. Mater. **1**, 16042 (2016).
[17] Y. Cao, V. Fatemi, S. Fang, K. Watanabe, T. Taniguchi, E. Kaxiras, and P. Jarillo-Herrero, Nature (London) **556**, 43 (2018).
[18] L. A. Ponomarenko, R. V. Gorbachev, G. L. Yu, D. C. Elias, R. Jalil, A. A. Patel, A. Mishchenko, A. S. Mayorov, C. R. Woods, J. R. Wallbank, M. Mucha-Kruczynski, B. A. Piot, M. Potemski, I. V. Grigorieva, K. S. Novoselov, F. Guinea, V. I. Fal'ko, and A. K. Geim, Nature (London) **497**, 594 (2013).
[19] G. Li, A. Luican, J. M. B. Lopes dos Santos, A. H. Castro Neto, J. K. A. Reina, and E. Y. Andrei, Nat. Phys. **6**, 109 (2009).
[20] X. Zhang and H. Luo, Appl. Phys. Lett. **103**, 231602 (2013).
[21] D. R. Hofstadter, Phys. Rev. B **14**, 2239 (1976).
[22] B. Hunt, J. D. Sanchez-Yamagishi, A. F. Young, M. Yankowitz, B. J. L. LeRoy, K. Watanabe, T. Taniguchi, P. Moon, M. Koshino, P. Jarillo-Herrero, and R. C. Ashoori, Science **340**, 1427 (2013).
[23] C. R. Dean, L. Wang, P. Maher, C. Forsythe, F. Ghahari, Y. Gao, J. Katoch, M. Ishigami, P. Moon, M. Koshino, T. Tanigushi, K. Watanabe, K. L. Shepard, J. Hone, and P. Kim, Nature (London) **497**, 598 (2013).
[24] P. Moon and M. Koshino, Phys. Rev. B **88**, 241412(R) (2013).
[25] G. L. Yu, R. V. Gorbachev, J. S. Tu, A. V. Kretinin, Y. Cao, R. Jalil, F. Withers, L. A. Ponomarenko, B. A. Piot, M. Potemski, D. C. Elias, X. Chen, K. Watanabe, T. Tanguchi, I. V. Grigorieva, K. S. Novoselov, V. I. Fal'ko, A. K. Geim, and A. Mishchenko, Nat. Phys. **10**, 525 (2014).
[26] S. J. Ahn, P. Moon, T.-H. Kim, H.-W. Kim, H.-C. Shin, E. H. Kim, H. W. Cha, S.-J. Kahng, P. Kim, M. Koshino, Y.-W. Son, C.-W. Yang, and J. R. Ahn, Science **361**, 782 (2018).
[27] W. Yao, E. Wang, C. Bao, Y. Zhang, K. Zhang, K. Bao, C. K. Chan, C. Chen, J. Avila, M. C. Asensio, J. Zhu, and S. Zhou, Proc. Natl. Acad. Sci. U.S.A. **115**, 6928 (2018).
[28] R. Decker, Y. Wang, V. W. Brar, W. Regan, H.-Z. Tsai, Q. Wu, W. Gannett, A. Zettl, and M. F. Crommie, Nano Lett. **11**, 2291 (2011).
[29] M. Yankowitz, J. Xue, D. Cormode, J. D. Sanchez-Yamagishi, K. Watanabe, T. Taniguchi, P. Jarillo-Herrero, P. Jacquod, and B. J. LeRoy, Nat. Phys. **8**, 382 (2012).
[30] J. R. Wallbank, M. Mucha-Kruczyński, X. Chen, and V. I. Fal'ko, Ann. Phys. (Berlin) **527**, 359 (2015).
[31] Q. Tong, H. Yu, Q. Zhu, Y. Wang, X. Xu, and W. Yao, Nat. Phys. **13**, 356 (2016).
[32] M. M. van Wijk, A. Schuring, M. I. Katsnelson, and A. Fasolino, 2D Mater. **2**, 034010 (2015).
[33] D. A. Cosma, J. R. Wallbank, V. Cheianov, and V. I. Fal'ko, Faraday Discuss. **173**, 137 (2014).
[34] M. Kuwabara, D. R. Clarke, and D. A. Smith, Appl. Phys. Lett. **56**, 2396 (1990).
[35] Z. Y. Rong and P. Kuiper, Phys. Rev. B **48**, 17427 (1993).
[36] K. Kobayashi, Phys. Rev. B **50**, 4749 (1994).
[37] U. Müller, D. Carnal, H. Siegenthaler, E. Schmidt, W. J. Lorenz, W. Obretenov, U. Schmidt, G. Staikov, and E. Budevski, Phys. Rev. B **46**, 12899(R) (1992).
[38] J. Coraux, A. T. N'Diaye, C. Busse, and T. Michely, Nano Lett. **8**, 565 (2008).
[39] L. Gao, J. R. Guest, and N. P. Guisinger, Nano Lett. **10**, 3512 (2010).
[40] J. C. Patrin, Y. Z. Li, M. Chander, and J. H. Weaver, Phys. Rev. B **46**, 10221 (1992).
[41] M. Pivetta, F. Patthey, M. Stengel, A. Baldereschi, and W.-D. Schneider, Phys. Rev. B **72**, 115404 (2005).
[42] P. Kang, W.-T. Zhang, V. Michaud-Rioux, X.-H. Kong, C. Hu, G.-H. Yu, and H. Guo, Phys. Rev. B **96**, 195406 (2017).

[43] P. J. Kowalczyk, O. Mahapatra, M. Le Ster, S. A. Brown, G. Bian, X. Wang, and T.-C. Chiang, Phys. Rev. B **96**, 205434 (2017).
[44] P. J. Kowalczyk, O. Mahapatra, D. Belić, S. A. Brown, G. Bian, and T.-C. Chiang, Phys. Rev. B **91**, 045434 (2015).
[45] T. Märkl, P. J. Kowalczyk, M. Le Ster, I. V. Mahajan, H. Pirie, Z. Ahmed, G. Bian, X. Wang, T.-C. Chiang, and S. A. Brown, 2D Mater. **5**, 011002 (2018).
[46] K. Kobayashi, Phys. Rev. B **53**, 11091 (1996).
[47] D. Hsieh, D. Qian, L. Wray, Y. Xia, Y. S. Hor, R. J. Cava, and M. Z. Hasan, Nature (London) **452**, 970 (2008).
[48] D. Hsieh, Y. Xia, L. Wray, D. Qian, A. Pal, J. H. Dil, J. Osterwalder, F. Meier, G. Bihlmayer, C. L. Kane, Y. S. Hor, R. J. Cava, and M. Z. Hasan, Science **323**, 919 (2009).
[49] Y. Lu, W. Xu, M. Zeng, G. Yao, L. Shen, M. Yang, Z. Luo, F. Pan, K. Wu, T. Das, P. He, J. Jiang, J. Martin, Y.-P. Feng, H. Lin, and X.-S. Wang, Nano Lett. **15**, 80 (2015).
[50] X. Wang, C. Xu, H. Hu, P. Wang, G. Bian, W. Tan, S. A. Brown, and T.-C. Chiang, Europhys. Lett. **119**, 27002 (2017).
[51] M. Wada, S. Murakami, F. Freimuth, and G. Bihlmayer, Phys. Rev. B **83**, 121310(R) (2011).
[52] S. Ito, B. Feng, M. Arita, A. Takayama, R.-Y. Liu, T. Someya, W.-C. Chen, T. Iimori, H. Namatame, M. Taniguchi, C.-M. Cheng, S.-J. Tang, F. Komori, K. Kobayashi, T.-C. Chiang, and I. Matsuda, Phys. Rev. Lett. **117**, 236402 (2016).
[53] F. Schindler, Z. Wang, M. G. Vergniory, A. M. Cook, A. Murani, S. Sengupta, A. Y. Kasumov, R. Deblock, S. Jeon, I. Drozdov, H. Bouchiat, S. Guéron, A. Yazdani, B. A. Bernevig, and T. Neupert, Nat. Phys. **14**, 918 (2018).
[54] S. A. Scott, M. V. Kral, and S. A. Brown, Surf. Sci. **587**, 175 (2005).
[55] D. N. McCarthy, D. Robertson, P. J. Kowalczyk, and S. A. Brown, Surf. Sci. **604**, 1273 (2010).
[56] P. J. Kowalczyk, O. Mahapatra, D. N. McCarthy, W. Kozlowski, Z. Klusek, and S. A. Brown, Surf. Sci. **605**, 659 (2011).
[57] P. J. Kowalczyk, D. Belic, O. Mahapatra, S. A. Brown, E. S. Kadantsev, T. K. Woo, B. Ingham, and W. Kozlowski, Appl. Phys. Lett. **100**, 151904 (2012).
[58] P. J. Kowalczyk, D. Belić, O. Mahapatra, and S. A. Brown, Acta Mater. **60**, 674 (2012).
[59] P. J. Kowalczyk, O. Mahapatra, S. A. Brown, G. Bian, X. Wang, and T.-C. Chian, Nano Lett. **13**, 43 (2013).
[60] P. J. Kowalczyk, O. Mahapatra, S. A. Brown, G. Bian, and T.-C. Chiang, Surf. Sci. **621**, 140 (2014).
[61] T. Nagao, J. T. Sadowski, M. Saito, S. Yaginuma, Y. Fujikawa, T. Kogure, T. Ohno, Y. Hasegawa, S. Hasegawa, and T. Sakurai, Phys. Rev. Lett. **93**, 105501 (2004).
[62] T. Hirahara, K. Miyamoto, I. Matsuda, T. Kadono, A. Kimura, T. Nagao, G. Bihlmayer, E. V. Chulkov, S. Qiao, K. Shimada, H. Namatame, M. Taniguchi, and S. Hasegawa, Phys. Rev. B **76**, 153305 (2007).
[63] H. R. Sharma, V. Fournée, M. Shimoda, A. R. Ross, T. A. Lograsso, P. Gille, and A. P. Tsai, Phys. Rev. B **78**, 155416 (2008).
[64] O. U. Aktürk, V. O. Özcelik, and S. Ciraci, Phys. Rev. B **91**, 235446 (2015).
[65] G. Wang, R. Pandey, and S. P. Karna, ACS Appl. Mater. Inter. **7**, 11490 (2015).
[66] M. Pumera and Z. Sofer, Adv. Mater. **29**, 1605299 (2017).
[67] S. K. Gupta, Y. Sonvane, G. Wang, and R. Pandey, Chem. Phys. Lett. **641**, 169 (2015).
[68] J. Ji, X. Song, J. Liu, Z. Yan, C. Huo, S. Zhang, M. Su, L. Liao, W. Wang, Z. Ni, Y. Hao, and H. Zeng, Nat. Commun. **7**, 13352 (2016).
[69] P. Ares, F. Aguilar-Galindo, D. Rodríguez-San-Miguel, D. A. Aldave, S. Díaz-Tendero, M. Alcamí, F. Martín, J. Gómez-Herrero, and F. Zamora, Adv. Mater. **28**, 6332 (2016).
[70] R. Flammini, S. Colonna, C. Hogan, S. K. Mahatha, M. Papagno, A. Barla, P. N. Sheverdyaeva, P. Moras, Z. S. Aliev, M. B. Babanly, E. V. Chulkov, C. Carbone, and F. Ronci, Nanotechology **29**, 065704 (2018).
[71] Z.-Q. Shi, H. Li, Q.-Q. Yuan, Y.-H. Song, Y.-Y. Lv, W. Shi, Z.-Y. Jia, L. Gao, Y.-B. Chen, W. Zhu, and S.-C. Li, Adv. Mater. **31**, 1806130 (2018).
[72] P. F. Zhang, Z. Liu, W. Duan, F. Liu, and J. Wu, Phys. Rev. B **85**, 201410 (2012).
[73] G. Yao, Z. Luo, W. Xu, Y. P. Feng, and X.-S. Wang, Sci. Rep. **3**, 2010 (2013).
[74] K. Zhao, Y.-F. Lv, S.-H. Ji, X. Ma, X. Chen, and Q.-K. Xue, J. Phys.: Condens. Matter **26**, 394003 (2014).
[75] K. Hermann, J. Phys.: Condens. Matter **24**, 314210 (2012).
[76] P. Hofmann, Prog. Surf. Sci. **81**, 191 (2006).
[77] R. Bonnet, A. Lherbier, C. Barraud, M. L. Della Rocca, P. Lafarge, and J.-C. Charlier, Sci. Rep. **6**, 19701 (2016).
[78] F. Varchon, P. Mallet, L. Magaud, and J.-Y. Veuillen, Phys. Rev. B **77**, 165415 (2008).
[79] H. S. Wong and C. Durkan, Phys. Rev. B **81**, 045403 (2010).
[80] F. Joucken, F. Frising, and R. Sporken, Carbon **83**, 48 (2015).
[81] K. Momma and F. Izumi, J. Appl. Crystallogr. **44**, 1272 (2011).
[82] P. Delhaes, *Graphite and Precursors* (CRC, Boca Raton, FL, 2000), p. 146.